

# Synergistic Manipulation of $\text{Zn}^{2+}$ Ion Flux and Desolvation Effect Enabled by Anodic Growth of a 3D $\text{ZnF}_2$ Matrix for Long-Lifespan and Dendrite-Free Zn Metal Anodes

Yang Yang, Chaoyue Liu, Zeheng Lv, Hao Yang, Yufei Zhang, Minghui Ye, Libao Chen, Jinbao Zhao, and Cheng Chao Li\*

Aqueous rechargeable Zn metal batteries have attracted widespread attention due to the intrinsic high volumetric capacity, low cost, and high safety. However, the low Coulombic efficiency and limited lifespan of Zn metal anodes resulting from uncontrollable growth of Zn dendrites impede their practical application. In this work, a 3D interconnected  $\text{ZnF}_2$  matrix is designed on the surface of Zn foil ( $\text{Zn@ZnF}_2$ ) through a simple and fast anodic growth method, serving as a multifunctional protective layer. The as-fabricated  $\text{Zn@ZnF}_2$  electrode can not only redistribute the  $\text{Zn}^{2+}$  ion flux, but also reduce the desolvation active energy significantly, leading to stable and facile Zn deposition kinetics. The results reveal that the  $\text{Zn@ZnF}_2$  electrode can effectively inhibit dendrites growth, restrain the hydrogen evolution reactions, and endow excellent plating/stripping reversibility. Accordingly, the  $\text{Zn@ZnF}_2$  electrode exhibits a long cycle life of over 800 h at  $1 \text{ mA cm}^{-2}$  with a capacity of  $1.0 \text{ mAh cm}^{-2}$  in a symmetrical cell test, the feasibility of which is also convincing in  $\text{Zn@ZnF}_2/\text{MnO}_2$  and  $\text{Zn@ZnF}_2/\text{V}_2\text{O}_5$  full batteries. Importantly, a hybrid zinc-ion capacitor of the  $\text{Zn@ZnF}_2/\text{AC}$  can work at an ultrahigh current density of  $\approx 60 \text{ mA cm}^{-2}$  for up to 5000 cycles with a high capacity retention of 92.8%.

Since the first commercialization in the 1990s, lithium-ion batteries (LIBs) have thoroughly changed our lives.<sup>[1]</sup> However, there is growing concern about the safety issues of LIBs owing to their high-profile fire or even explosion accidents in cell phones, electric vehicles, and aeroplanes associated with the toxic and flammable organic electrolytes.<sup>[2]</sup> To

date, aqueous rechargeable batteries are gaining increasing attention as a safer electrochemical energy storage technology based on non-flammable and high ion conductivity aqueous electrolytes.<sup>[3]</sup> Among various aqueous battery chemistries, zinc-ion batteries (ZIBs) have garnered the greatest interest due to the merits of Zn metal deriving from its high specific capacity (volumetric capacity of  $5855 \text{ mAh cm}^{-3}$  and gravimetric capacity of  $820 \text{ mAh g}^{-1}$ ), low reduction potential ( $-0.76 \text{ V}$  vs standard hydrogen electrode), low cost and high abundance.<sup>[4]</sup> Unfortunately, Zn metal anode in mild electrolyte still suffers from problems including severe corrosion reactions, hydrogen evolution and uncontrolled formation of Zn dendrites, which results in low Coulombic efficiency (CE), poor cycle life, and even the internal short-circuit.<sup>[5]</sup>


Tremendous efforts have been exerted to solve the aforementioned problems of Zn metal anode. In terms of electrolytes,

various additives such as polyacrylamide (PAM),<sup>[6]</sup> nickel triflate,<sup>[7]</sup> ethylene glycol,<sup>[8]</sup> benzyltrimethylammonium hydroxide (BTMAH),<sup>[9]</sup> dodecyltrimethylammonium bromide (DTAB),<sup>[10]</sup> methyl ester ethoxylate (FMEE)<sup>[11]</sup> and diethyl ether<sup>[12]</sup> have been studied as an effective approach to suppress Zn dendrite growth. Besides, high concentration electrolytes such as  $20 \text{ M LiTFSI} + 1 \text{ M Zn(TFSI)}_2$ ,<sup>[13]</sup>  $30 \text{ M ZnCl}_2$ ,<sup>[14]</sup> and “water-mixed deep eutectic solvent” electrolytes<sup>[15]</sup> have been also proposed. Because there is less free water contained in the high-concentration electrolyte compared with conventional dilute aqueous electrolyte, which may efficiently reduce the formation of Zn dendrites and water-induced Zn corrosion. Nonetheless, the greatly excessive amount of electrolyte salts would lead to increased material cost and total battery weight. Recently, more studies have been focused on the modification of the interface between Zn metal anode and liquid electrolyte. For instance, Cui et al. designed a polymeric interphase layer composed of polyamide and  $\text{Zn(TfO)}_2$ , which can not only regulate Zn deposition, but also protect the surface of the deposited Zn from the electrolyte.<sup>[16]</sup> Besides, constructing coating layers including metal-organic frameworks (MOFs),<sup>[17]</sup> nanoporous  $\text{CaCO}_3$ ,<sup>[18]</sup> poly(vinyl butyral),<sup>[19]</sup>  $\text{ZnO}$ ,<sup>[20]</sup>  $\text{ZnS}$ ,<sup>[21]</sup> carbon black,<sup>[22]</sup>

Dr. Y. Yang, Z. H. Lv, Dr. Y. F. Zhang, Dr. M. H. Ye, Prof. C. C. Li  
School of Chemical Engineering and Light Industry  
Guangdong University of Technology  
Guangzhou 510006, P. R. China  
E-mail: licc@gdut.edu.cn

C. Y. Liu, Prof. J. B. Zhao  
College of Chemistry and Chemical Engineering  
Xiamen University  
Xiamen 361005, P. R. China

H. Yang, Prof. L. B. Chen  
State Key Laboratory for Powder Metallurgy  
Central South University  
Changsha 410083, P. R. China

 The ORCID identification number(s) for the author(s) of this article can be found under <https://doi.org/10.1002/adma.202007388>.

DOI: 10.1002/adma.202007388

indium-based compounds<sup>[23]</sup> and TiO<sub>2</sub>/PVDF composite<sup>[24]</sup> have also been proved to be effective in delaying Zn dendrite formation and improving electrochemical performance. However, these protective layers may be cracked during long-term cycling especially at high current densities due to the drastic volume change during Zn deposition/stripping. Therefore, rather than simply suppressing or delaying Zn dendrite growth, new strategies are highly needed to tackle the inherent drawbacks of Zn metal anode.

From a fundamental point of view, two underlying factors should be carefully considered to build an in-depth understanding of the reversibility and stability concerns of Zn metal anode. First, the nonuniform Zn<sup>2+</sup> ion flux resulting from inhomogeneous electric field distribution and concentration polarization is the main reason for the formation of dendritic Zn.<sup>[21,25]</sup> Besides, the large desolvation penalty of Zn deposition at the electrode–electrolyte is undesirable for facile deposition kinetics. Because a large energy consumption related to the desolvation process of [Zn(H<sub>2</sub>O)<sub>6</sub>]<sup>2+</sup> in the aqueous electrolyte is required owing to its strong Coulombic interaction with the H<sub>2</sub>O solvation sheath, which may trigger the hydrogen evolution reactions.<sup>[26]</sup> The production of H<sub>2</sub> is accompanied by a localized pH increase near the reaction interphase and eventually promotes the generation of hydroxide sulfate Zn compounds, which are called “dead Zn” owing to the electronic insulator and non-electroactive properties of deposits.<sup>[8]</sup> Herein, a 3D interconnected ZnF<sub>2</sub> matrix is proposed as a multifunctional protective layer to overcome the above two key issues simultaneously. The as-fabricated Zn@ZnF<sub>2</sub> electrode can efficiently redistribute the Zn<sup>2+</sup> ion flux and significantly reduce the desolvation active energy, leading to stable and facile Zn deposition kinetics. Benefiting from the manipulated Zn deposition behavior, the Zn@ZnF<sub>2</sub> electrode was demonstrated to effectively inhibit dendrites growth, restrain the hydrogen evolution reactions, and endow excellent plating/stripping stability. Consequently, the as-fabricated Zn@ZnF<sub>2</sub> electrode delivers high Coulombic efficiency (≈99.5%) and ultralong lifespan (800 h) with a relatively high plating capacity of 1 mAh cm<sup>-2</sup>.

The 3D interconnected ZnF<sub>2</sub> matrix was potentiostatically electrodeposited onto a Zn foil substrate in an aqueous solution containing 1.0 M NH<sub>4</sub>F (Figure 1a). Once a constant voltage of 15 V is applied between the two electrodes, a large amount of Zn<sup>2+</sup> ions are generated near the inner Helmholtz plane via the anodic reaction (Zn → Zn<sup>2+</sup> + 2e<sup>-</sup>), and then the Zn<sup>2+</sup> cations react with F<sup>-</sup> anions from the electrolyte, forming a ZnF<sub>2</sub> matrix with a thickness of ≈9.3 μm on the surface of Zn foil. Besides, the thickness of ZnF<sub>2</sub> coating layer can be controlled by changing the reaction time (Figure S1, Supporting Information). Even after being curved, the Zn@ZnF<sub>2</sub> electrode is capable of accommodating the bending without the appearance of cracks, indicating the excellent mechanical strength (Figure S2a, Supporting Information). Moreover, the tape tested for the Zn@ZnF<sub>2</sub> electrode shows no noticeable particles (Figure S2b,c, Supporting Information), revealing the strong adhesion between the ZnF<sub>2</sub> coating layer and Zn substrate. The crystalline structure and chemical composition of the depositing film were further confirmed by XRD (X-ray diffraction) and XPS (X-ray photoelectron spectroscopy) measurements (Figure 1b,c). As shown in Figure 1b, a new phase was detected

in the Zn@ZnF<sub>2</sub> electrode compared with the pristine Zn foil after the electrochemical anodic growth. However, the crystallinity degree of the resulting ZnF<sub>2</sub> matrix may be poor, three weak diffractions peaks located at 26.75°, 34.47° and 52.13° can be assigned to the (110), (101), and (211) planes of tetragonal ZnF<sub>2</sub> (JCPDS No. 01-0661), respectively. In the XPS spectra, the pristine Zn foil only exhibits the binding energies of Zn 2p<sub>3/2</sub> and Zn 2p<sub>1/2</sub> at 1022.3 and 1045.4 eV, respectively (Figure S3, Supporting Information), whereas the Zn@ZnF<sub>2</sub> electrode shows obvious F signals of F 1s at 684.4 eV (Figure 1c), which corresponds to the characteristic XPS band of ZnF<sub>2</sub>.<sup>[27]</sup> The wettability between electrode and electrolyte plays a crucial role in the Zn deposition behavior, because the electrode with good wettability can efficiently retain the electrolyte and enhance the uniform distribution of Zn<sup>2+</sup> ions at the interface. Figure 1d displays the contact angle on the pristine Zn foil and Zn@ZnF<sub>2</sub> electrode for 2 M ZnSO<sub>4</sub> aqueous electrolyte. A small contact angle reveals good wetting performance while poor wetting is indicated by a large contact angle. As can be seen from the figure, the contact angle of the Zn@ZnF<sub>2</sub> electrode (47.3°) is significantly reduced than that of the pristine Zn foil (75.9°), which may be associated with the stronger interaction between electrolyte and ZnF<sub>2</sub>.

SEM images of both the Zn foil and Zn@ZnF<sub>2</sub> electrode were obtained to elucidate the morphology evolution after the electrochemical anodic growth. As shown in Figure 1e,f, there are many scratches observed on the surface of the Zn foil, which may be formed during its manufacturing process.<sup>[28]</sup> These scratches increase the surface roughness and enhance the tip electric field density, aggravating the formation of Zn dendrites during cycling. SEM images of the Zn@ZnF<sub>2</sub> electrode (Figure 1g,h) display that the surface of the Zn substrate is tightly covered with a continuous and dense ZnF<sub>2</sub> matrix with interconnected 3D morphology, which can increase the contact area of electrode/electrolyte and afford abundant porous tunnels for ion transport. Furthermore, EDX mapping images (Figure 1i) show that Zn and F elements are homogeneously distributed on the surface, demonstrating the uniformity of ZnF<sub>2</sub> matrix. To further confirm the existence of ZnF<sub>2</sub> phase, the ZnF<sub>2</sub> film was scraped from the substrate using a scalpel and investigated by TEM (Figure S4, Supporting Information). As shown in Figure S4a, Supporting Information, many small pores are observed in the ZnF<sub>2</sub> film. The HR-TEM image of the ZnF<sub>2</sub> film (Figure S4b, Supporting Information) shows indistinct lattice fringes, confirming the low crystallinity degree. The interplanar distance in the enlarged section (inset in Figure S4b, Supporting Information) is ≈0.26 nm, matching well with the (110) plane of tetragonal ZnF<sub>2</sub>. Furthermore, the selected-area electron diffraction pattern of the ZnF<sub>2</sub> film (Figure S4c, Supporting Information) exhibits faint diffraction rings, which can be assigned to (110), (101), (111), (211), and (310) planes of polycrystalline ZnF<sub>2</sub>, respectively. The element mapping images (Figure S4d–f, Supporting Information) reveal that Zn and F elements are homogeneously distributed in the ZnF<sub>2</sub> film.

The ZnF<sub>2</sub> matrix grown on the surface of the Zn substrate is expected to act as a protective coating layer to inhibit the corrosion of Zn metal anode in aqueous electrolyte. After immersed in 2 M aqueous ZnSO<sub>4</sub> electrolyte for one week, the Zn foil obviously tarnished and formed many small pits on the surface,

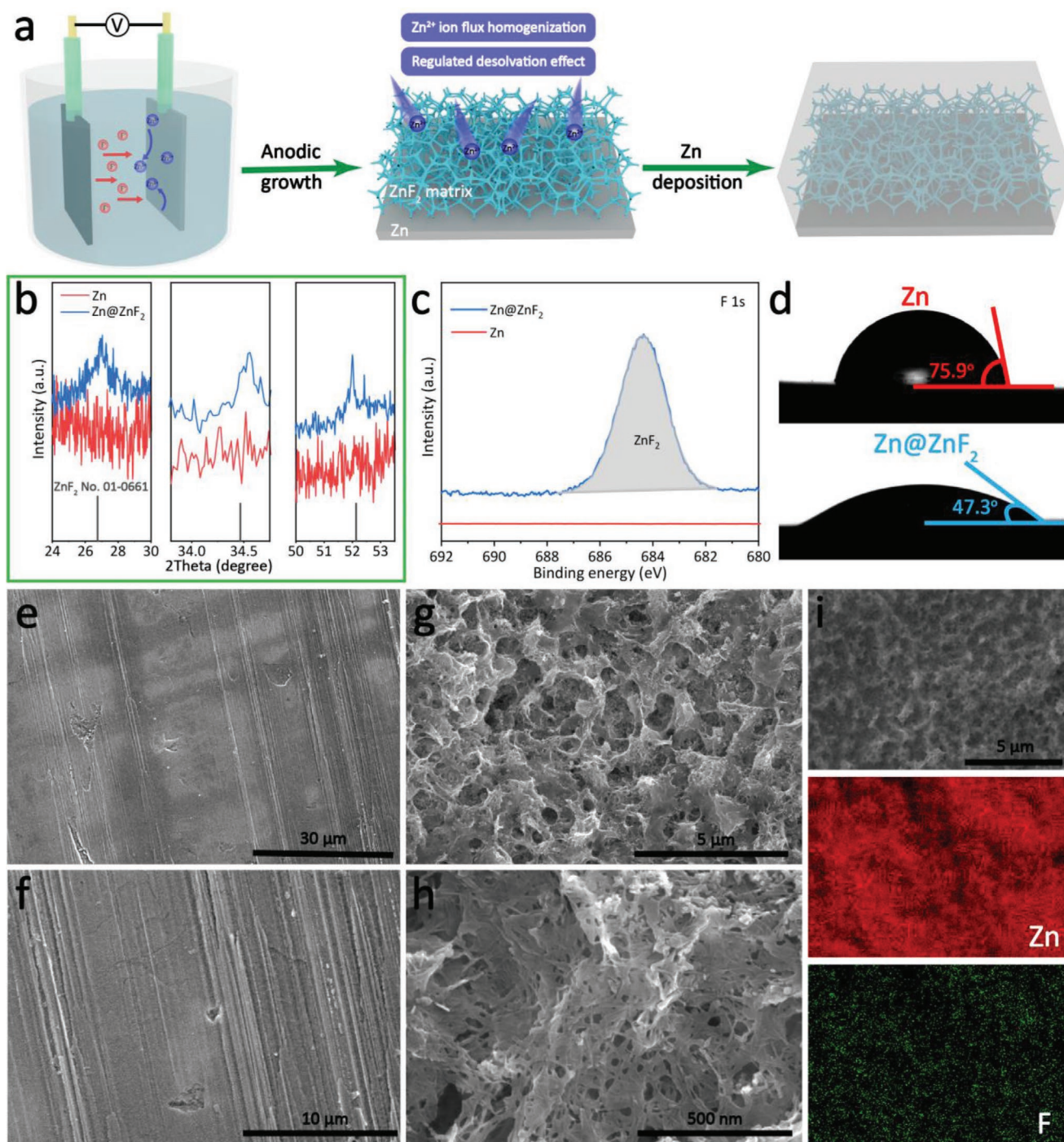


**Figure 1.** a) Schematic illustration of the fabrication of the Zn@ZnF<sub>2</sub> electrode. b) XRD patterns and c) high-resolution F 1s XPS spectra of the pristine Zn foil and Zn@ZnF<sub>2</sub> electrode. d) Contact angles of 2 m ZnSO<sub>4</sub> aqueous solution on the pristine Zn foil and Zn@ZnF<sub>2</sub> electrode. e–h) SEM images of the pristine Zn foil (e,f) and the Zn@ZnF<sub>2</sub> electrode (g,h). i) SEM image and corresponding elemental mapping of the surface of the Zn@ZnF<sub>2</sub> electrode.

resulting from severe corrosion reactions between Zn metal and electrolyte (Figure 2a). By contrast, the Zn@ZnF<sub>2</sub> electrode exhibited no visible morphology change, revealing the better chemical stability in the electrolyte. The corrosion-resistant performance was further quantitatively studied by the linear polarization experiments (Figure 2b). The corrosion potential ( $E_{\text{corr}}$ ) of the Zn@ZnF<sub>2</sub> electrode (−1.014 V vs saturated calomel

electrode (SCE)) is more positive than that of Zn foil (−1.022 V vs SCE). In addition, the corrosion current density ( $i_{\text{corr}}$ ) is a more direct factor in evaluating the rate of self-corrosion reactions. Here,  $i_{\text{corr}}$  of the Zn@ZnF<sub>2</sub> electrode (0.28 mA cm<sup>−2</sup>) is much reduced comparing with that of Zn foil (0.86 mA cm<sup>−2</sup>). These results reveal that the anodic dissolution and hydrogen evolution reaction are effectively suppressed in the existence of ZnF<sub>2</sub>



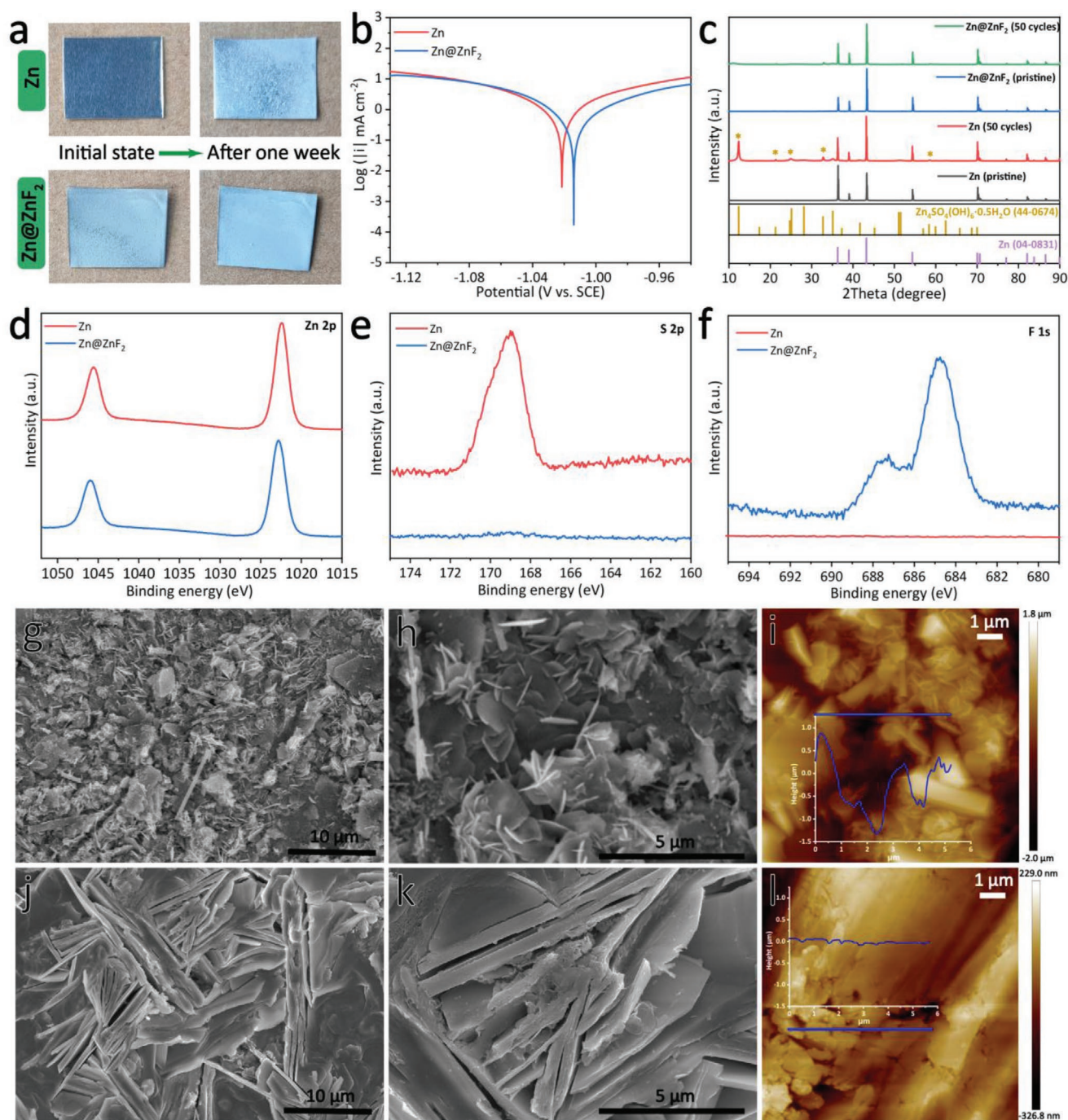


**Figure 2.** a) Optical images of the Zn foil and Zn@ZnF<sub>2</sub> electrode in initial state and immersed in 2 m aqueous ZnSO<sub>4</sub> electrolyte for one week. b) The potentiodynamic polarization curves of the Zn foil and Zn@ZnF<sub>2</sub> electrode in 2 m ZnSO<sub>4</sub> aqueous solution. c) XRD patterns and d–f) XPS analysis of the Zn foil and Zn@ZnF<sub>2</sub> electrode after 50 cycles. g,h) SEM images and i) AFM image of the Zn foil after 50 cycles. j–k) SEM images and l) AFM image of the Zn@ZnF<sub>2</sub> electrode after 50 cycles (insets show the corresponding height profiles for the blue line segments).

protective layer. In a mild acidic ZnSO<sub>4</sub> aqueous electrolyte, the hydrogen evolution is destructive, which will not only damage the electrode architecture but also trigger side reactions between Zn and electrolyte that consuming Zn<sup>2+</sup> ions irreversibly. Since the local OH<sup>−</sup> anions will accumulate while the H<sup>+</sup> cations reacted with the Zn to release H<sub>2</sub>, and the high concentration of OH<sup>−</sup> anions immediately react with ZnSO<sub>4</sub> to produce hydrate

Zn compounds on the surface of Zn. The effectively inhibited hydrogen evolution reaction of the Zn@ZnF<sub>2</sub> electrode is in favor of reducing the generation of Zn<sub>4</sub>SO<sub>4</sub>(OH)<sub>6</sub>·xH<sub>2</sub>O byproducts. To test this hypothesis, the Zn foil and Zn@ZnF<sub>2</sub> electrode were disassembled from symmetric batteries and examined after 50 cycles at 1.0 mA cm<sup>−2</sup>. As shown in Figure 2c, strong peaks corresponding to Zn<sub>4</sub>SO<sub>4</sub>(OH)<sub>6</sub>·0.5H<sub>2</sub>O byproducts can

be clearly observed in the Zn foil after 50 cycles. In comparison, no obvious peaks of  $\text{Zn}_4\text{SO}_4(\text{OH})_6 \cdot 0.5\text{H}_2\text{O}$  or other byproducts are detected in the  $\text{Zn}@\text{ZnF}_2$  electrode after 50 cycles. To obtain more convincing evidence, we also characterized the electrode after 50 cycles using XPS (Figure 2d–f). Both the Zn foil and  $\text{Zn}@\text{ZnF}_2$  electrode show two Zn  $2p_{1/2}$  and Zn  $2p_{3/2}$  peaks in the Zn 2p spectra (Figure 2d). In the S 2p spectra, a strong peak at 169.0 eV indicates the presence of  $\text{Zn}_4\text{SO}_4(\text{OH})_6 \cdot 0.5\text{H}_2\text{O}$  for the Zn foil after 50 cycles (Figure 2e). In sharp contrast, there are no apparent peaks appearing in the range of 160–175 eV for the  $\text{Zn}@\text{ZnF}_2$  electrode, demonstrating the nonexistence of  $\text{Zn}_4\text{SO}_4(\text{OH})_6 \cdot 0.5\text{H}_2\text{O}$  byproducts. It is worth noting that strong F signals can be still identified in the F 1s spectra for the  $\text{Zn}@\text{ZnF}_2$  electrode (Figure 2f), implying that the  $\text{ZnF}_2$  matrix can be well maintained during prolonged cycling.

After 50 cycles, ultrathin hexagonal platelets with a diameter of only 1–2  $\mu\text{m}$  are stacked randomly on the surface of the Zn foil (Figure 2g,h), in agreement with the previously reported results.<sup>[29]</sup> The uneven and loose distribution of flakey Zn dendrites may cause the inhomogeneity of the electric field and  $\text{Zn}^{2+}$  ion concentration at the interface, further exacerbating the growth of dendrites. SEM images of the  $\text{Zn}@\text{ZnF}_2$  electrode shows a much denser deposition morphology, neither ultrathin nanoflake nor mossy-like dendrites are observed (Figure 2j,k and Figure S5, Supporting Information). Instead, Zn metal grew to micro-sized sheets up to 30  $\mu\text{m}$  in size, which were tightly packed to form a compact morphology. Moreover, AFM and the inset height fluctuation images (Figure 2i–l) clearly reveal that the surface of the  $\text{Zn}@\text{ZnF}_2$  electrode is much smoother than that of the Zn foil after 50 cycles.

The electrochemical characterization of the electrodes for Zn deposition/stripping is displayed in Figure 3. The CE is an important index to evaluate the reversibility of Zn during repeated cycling, which was measured by assembling  $\text{Cu}||\text{Zn}$  and  $\text{Cu}@\text{ZnF}_2||\text{Zn}$  half cells and cycled with a plating capacity of 1  $\text{mAh cm}^{-2}$  at a current density of 5  $\text{mA cm}^{-2}$ , and then charged to 0.5 V (vs  $\text{Zn}^{2+}/\text{Zn}$ ). Here, a  $\text{ZnF}_2$  coating layer was introduced onto the Cu foil by the conventional slurry casting method. The  $\text{Cu}||\text{Zn}$  half cell shows a gradual rise in voltage hysteresis, and increases to 122.7 mV after 250 cycles (Figure 3a). While for the  $\text{Cu}@\text{ZnF}_2||\text{Zn}$  half cell, it exhibits a prominently lower voltage hysteresis of  $\approx 84.9$  mV and maintains steadily up to 1000 cycles. Furthermore, the  $\text{Cu}@\text{ZnF}_2||\text{Zn}$  half cell can deliver an average CE of above 99.5% for over 1000 cycles at 5  $\text{mA cm}^{-2}$  with a capacity of 1  $\text{mAh cm}^{-2}$  (Figure 3c). However, the CE of the  $\text{Cu}||\text{Zn}$  half cell underwent a drastic degradation after 250 cycles, due to the continuous formation of dead Zn. The CEs of the  $\text{Cu}@\text{ZnF}_2||\text{Zn}$  half cell at lower current densities was also tested (Figure S6, Supporting Information). The average CEs of  $\text{Cu}@\text{ZnF}_2||\text{Zn}$  half cells are 98.6% after 200 cycles at 0.5  $\text{mA cm}^{-2}$ , and 99.2% after 800 cycles at 2  $\text{mA cm}^{-2}$ . Figure 3d–f shows the voltage hysteresis of symmetric  $\text{Zn}||\text{Zn}$  and  $\text{Zn}@\text{ZnF}_2||\text{Zn}@\text{ZnF}_2$  cells at 0.5, 1.0, and 10  $\text{mA cm}^{-2}$ , respectively. As shown in Figure 3d, the  $\text{Zn}@\text{ZnF}_2||\text{Zn}@\text{ZnF}_2$  cell displayed stable voltage profiles with a small hysteresis beyond 500 h at 0.5  $\text{mA cm}^{-2}$ . Whereas the voltage hysteresis of the  $\text{Zn}||\text{Zn}$  cell fluctuated after only 70 h, as a result of dendrite-induced internal short-circuit of batteries. Under the high current density of 10  $\text{mA cm}^{-2}$ , the deviations

in cycling stability between these two electrodes became more evident (Figure 3e). A sudden voltage drop and drastic voltage fluctuation were observed after 125 h in the  $\text{Zn}||\text{Zn}$  cell. In contrast, the  $\text{Zn}@\text{ZnF}_2||\text{Zn}@\text{ZnF}_2$  cell can still keep working over 500 h. When cycled for a larger plating/stripping capacity of 2  $\text{mAh cm}^{-2}$  at 10  $\text{mA cm}^{-2}$ , the voltage hysteresis of  $\text{Zn}@\text{ZnF}_2||\text{Zn}@\text{ZnF}_2$  symmetrical cell also maintain stably at a relatively low value of  $\approx 79.6$  mV (Figure S7, Supporting Information). Of note, an ultralong cycle life of 800 h has been achieved for the  $\text{Zn}@\text{ZnF}_2||\text{Zn}@\text{ZnF}_2$  cell at 1.0  $\text{mA cm}^{-2}$  with a plating capacity of 1.0  $\text{mAh cm}^{-2}$  (Figure 3f). Furthermore, the voltage hysteresis of Zn plating/stripping in the  $\text{Zn}@\text{ZnF}_2$  electrode is always stable and maintained at  $\approx 71.5$  mV, which is lower than that of the Zn foil (128.0 mV) at the early stage.

Numerical simulations of the  $\text{Zn}^{2+}$  flux distribution for the Zn foil and  $\text{Zn}@\text{ZnF}_2$  electrode were performed to understand the differences in deposition behavior (Figure 4a,b). The surface of the Zn foil is uneven and rough, and the  $\text{Zn}^{2+}$  flux near the protruding Zn nuclei is determined to be substantially enhanced. The inhomogeneous distribution of the  $\text{Zn}^{2+}$  flux on the surface of Zn foil generates Zn deposition “hot spots” (small isolated red regions in the blue background), resulting in the formation of Zn dendrites. After building a 3D  $\text{ZnF}_2$  matrix on the surface of the Zn substrate, the magnitude of  $\text{Zn}^{2+}$  flux in the whole electrode architecture is simultaneously enhanced and homogenized (Figure 4b). Moreover, no “hot spots” are visible near the protruding Zn nuclei, demonstrating that significant variations in the  $\text{Zn}^{2+}$  flux magnitude are effectively restrained, which should lead to the uniform Zn deposition. Interestingly, the roughness of the protruding Zn nuclei can be even improved during the Zn deposition process, which is seen in the dynamic Zn deposition simulation of the  $\text{Zn}@\text{ZnF}_2$  electrode (Video S1, Supporting Information). Additionally, we also built a physical model with a curved  $\text{ZnF}_2$  matrix (Figure S8, Supporting Information), the distribution of  $\text{Zn}^{2+}$  flux in tortuous ion channels is also effectively homogenized. The higher magnitude of  $\text{Zn}^{2+}$  flux on the surface of the  $\text{Zn}@\text{ZnF}_2$  electrode compared with the Zn foil should lead to the more facile Zn deposition kinetics, which may be associated with the improvement of the desolvation effect. It is well known that  $\text{Zn}^{2+}$  ions face large desolvation penalties at the electrode-electrolyte interface owing to the strong Coulombic interactions between the solvated divalent ion and its surrounding solvent shell.<sup>[5a,30]</sup> Therefore, the desolvation process of  $\text{Zn}^{2+}$  ions is usually considered to be the rate-limiting procedure for Zn deposition at the anode, which can be described by the activation energy ( $E_a$ ) through the law of Arrhenius equation<sup>[20b,31]</sup>

$$1/R_{ct} = A \exp(-E_a/RT) \quad (1)$$

where  $R_{ct}$  is the interfacial resistance,  $A$  is the frequency factor,  $R$  is the gas constant, and  $T$  is the absolute temperature. Figure 4c,d show EIS of the Zn foil and  $\text{Zn}@\text{ZnF}_2$  electrode at various temperatures ranging from 30 to 80 °C. The  $R_{ct}$  of the  $\text{Zn}@\text{ZnF}_2$  electrode (294.9  $\Omega$ ) at 30 °C is reduced by almost 6 times, compared with a much larger  $R_{ct}$  of the Zn foil (2021.0  $\Omega$ ), confirming the improved charge transfer capability. As shown in Figure 4e, the  $E_a$  for the  $\text{Zn}@\text{ZnF}_2$  electrode is about 39.1  $\text{kJ mol}^{-1}$ , which is much lower than that for the Zn



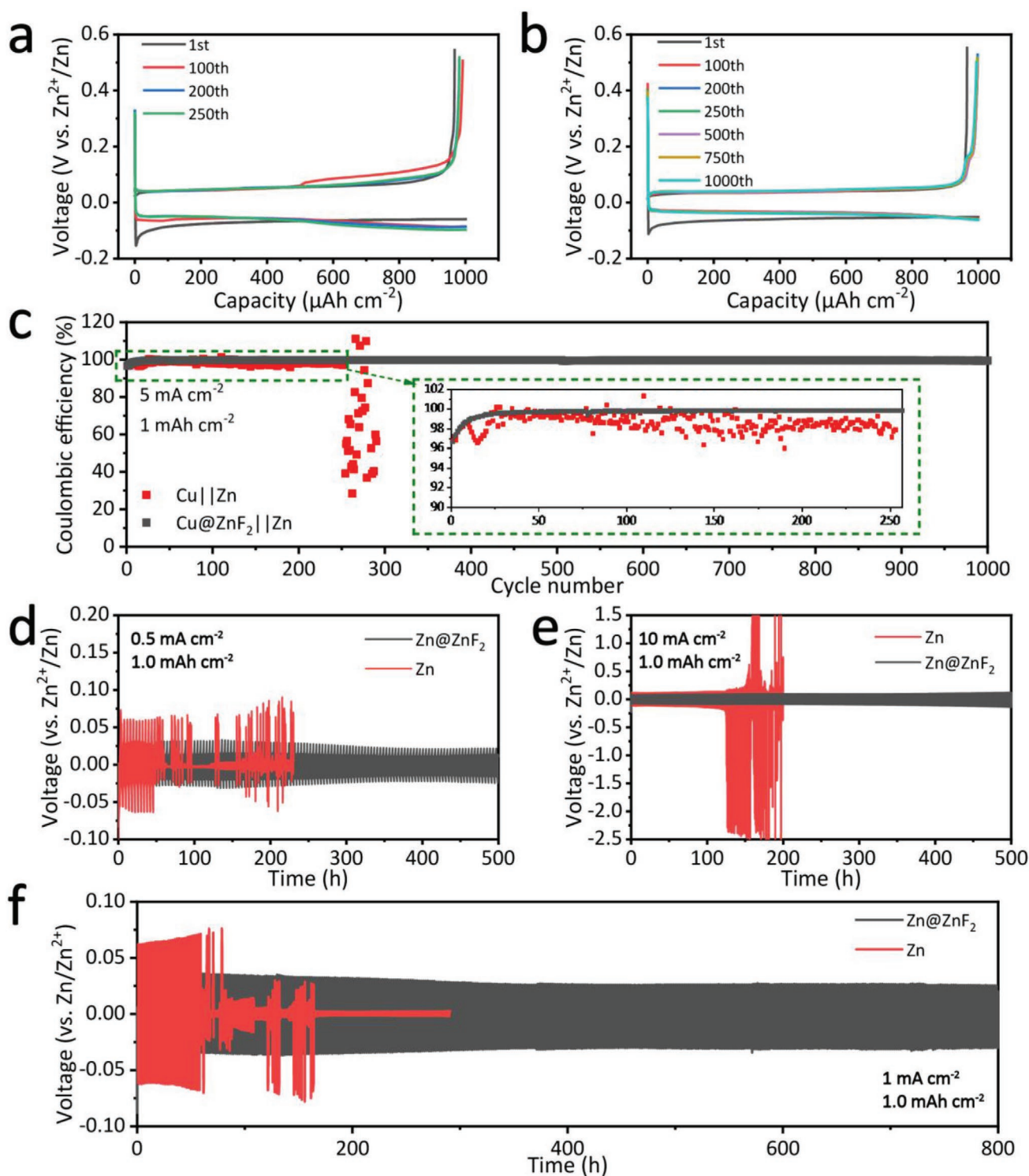


**Figure 3.** Electrochemical characterization of the electrodes for Zn deposition/stripping. a,b) Galvanostatic voltage profiles of Cu||Zn (a) and Cu@ZnF<sub>2</sub>||Zn (b) half cells at 5 mA cm<sup>-2</sup> with a plating capacity of 1 mAh cm<sup>-2</sup>. c) Coulombic efficiency of Cu||Zn and Cu@ZnF<sub>2</sub>||Zn half cells at 5 mA cm<sup>-2</sup> and a Zn plating capacity of 1 mAh cm<sup>-2</sup>. d–f) The time–voltage curves for Zn||Zn and Zn@ZnF<sub>2</sub>||Zn@ZnF<sub>2</sub> symmetrical cells at 0.5 mA cm<sup>-1</sup> (d), 10 mA cm<sup>-1</sup> (e), and 1 mA cm<sup>-1</sup> (f) with a plating/stripping capacity of 1 mAh cm<sup>-2</sup>.

foil (70.6 kJ mol<sup>-1</sup>). The decreased energy barrier proves that the strong polar nature of ZnF<sub>2</sub> matrix has a positive effect on the removal of Zn<sup>2+</sup> solvation sheath and promotes facile ion

transfer kinetics. It is worth mentioning that this relatively low value of 39.1 kJ mol<sup>-1</sup> is even compared to the desolvation activation energies in the monovalent lithium ion battery

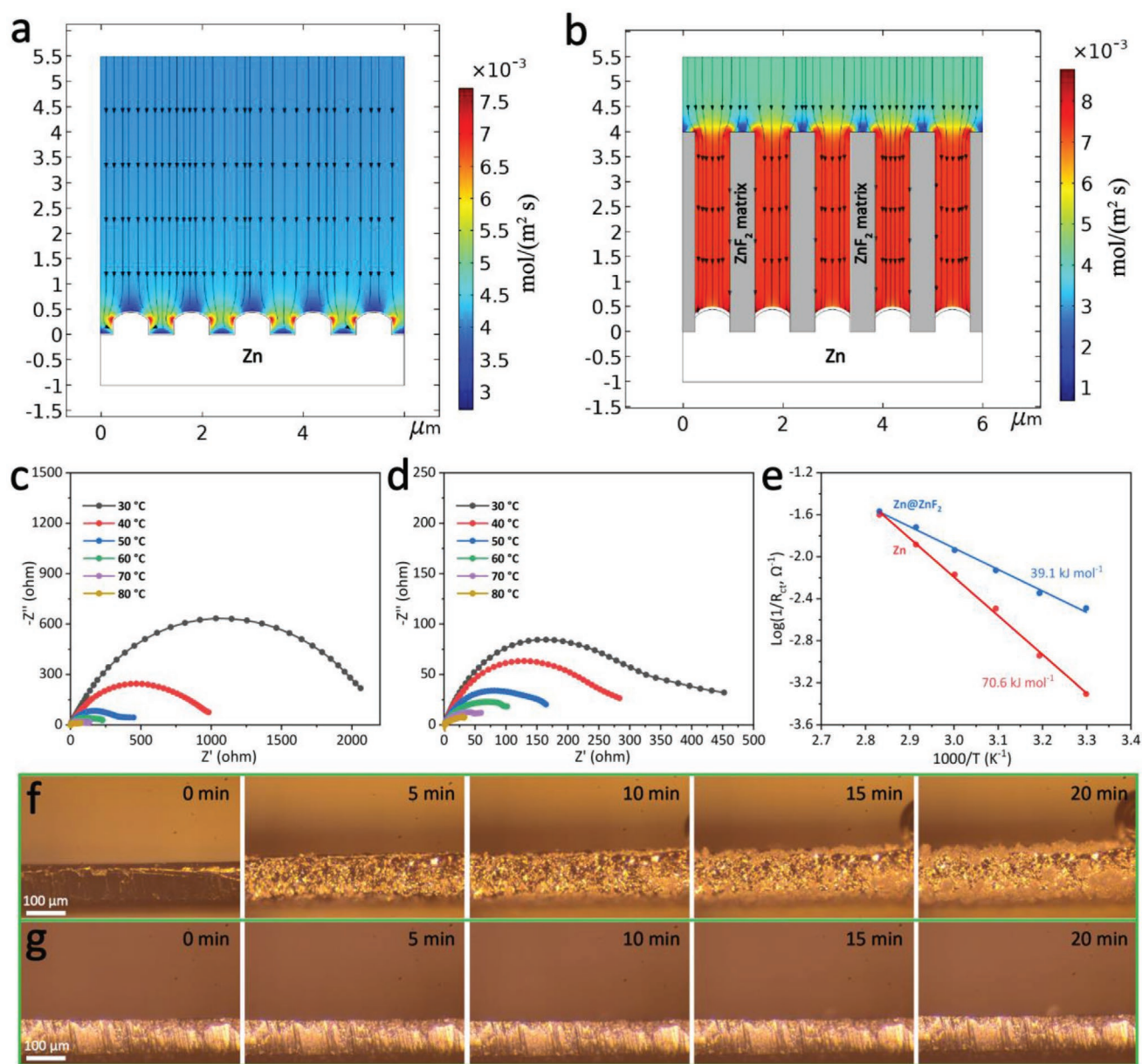


**Figure 4.** a,b) Numerical simulation of the  $\text{Zn}^{2+}$  flux distribution during deposition on the Zn foil (a) and on the  $\text{Zn}@\text{ZnF}_2$  electrode (b). c,d) EIS of the Zn foil (c) and the  $\text{Zn}@\text{ZnF}_2$  electrode (d) at different temperatures. e) The calculated desolvation activation energies of both electrodes by using the Arrhenius equation. f,g) In situ optical observation results of the Zn deposition morphologies on the Zn foil (f) and on the  $\text{Zn}@\text{ZnF}_2$  electrode (g) at a current density of 10  $\text{mA cm}^{-2}$  for 20 min.

system (50–60  $\text{kJ mol}^{-1}$ ). To probe the interactions between the Zn atom and Zn metal or  $\text{ZnF}_2$ , the calculation of binding energy was performed based on density functional theory (DFT). As shown in Figure S9, Supporting Information, the binding energy of  $\text{Zn}-\text{ZnF}_2$  (−6.40 eV) is much more negative than that of  $\text{Zn}-\text{Zn}$  metal (−1.27 eV), indicating the strong interaction between Zn atom and  $\text{ZnF}_2$ . Therefore, the  $\text{ZnF}_2$  matrix exhibits high Coulombic attraction toward  $\text{Zn}^{2+}$ , which facilitates the removal of solvation sheath in  $[\text{Zn}(\text{H}_2\text{O})_6]^{2+}$  during cycling.

An optical microscope was applied to obtain in situ photographs during the Zn metal plating process on the Zn foil and  $\text{Zn}@\text{ZnF}_2$  electrode (Figure 4f,g). Small and loose Zn

particles growing on the Zn foil are clearly visible within 5 min, and accumulate into the mossy-like dendrites after 20 min (Figure 4f and Video S2, Supporting Information). In addition, a small bubble resulting from the hydrogen evolution reaction is observed after 10 min, and keeps growing, after 20 min, into a big one with the diameter of  $\approx 100 \mu\text{m}$ . Comparatively, the interface between electrode and electrolyte remains smooth, and no such dendrite or bubble can be found on the  $\text{Zn}@\text{ZnF}_2$  electrode during Zn plating for 20 min (Figure 4g and Video S3, Supporting Information).

To explore the feasibility of the  $\text{Zn}@\text{ZnF}_2$  electrode for practical application,  $\text{MnO}_2$  and  $\text{V}_2\text{O}_5$  were employed as cathode

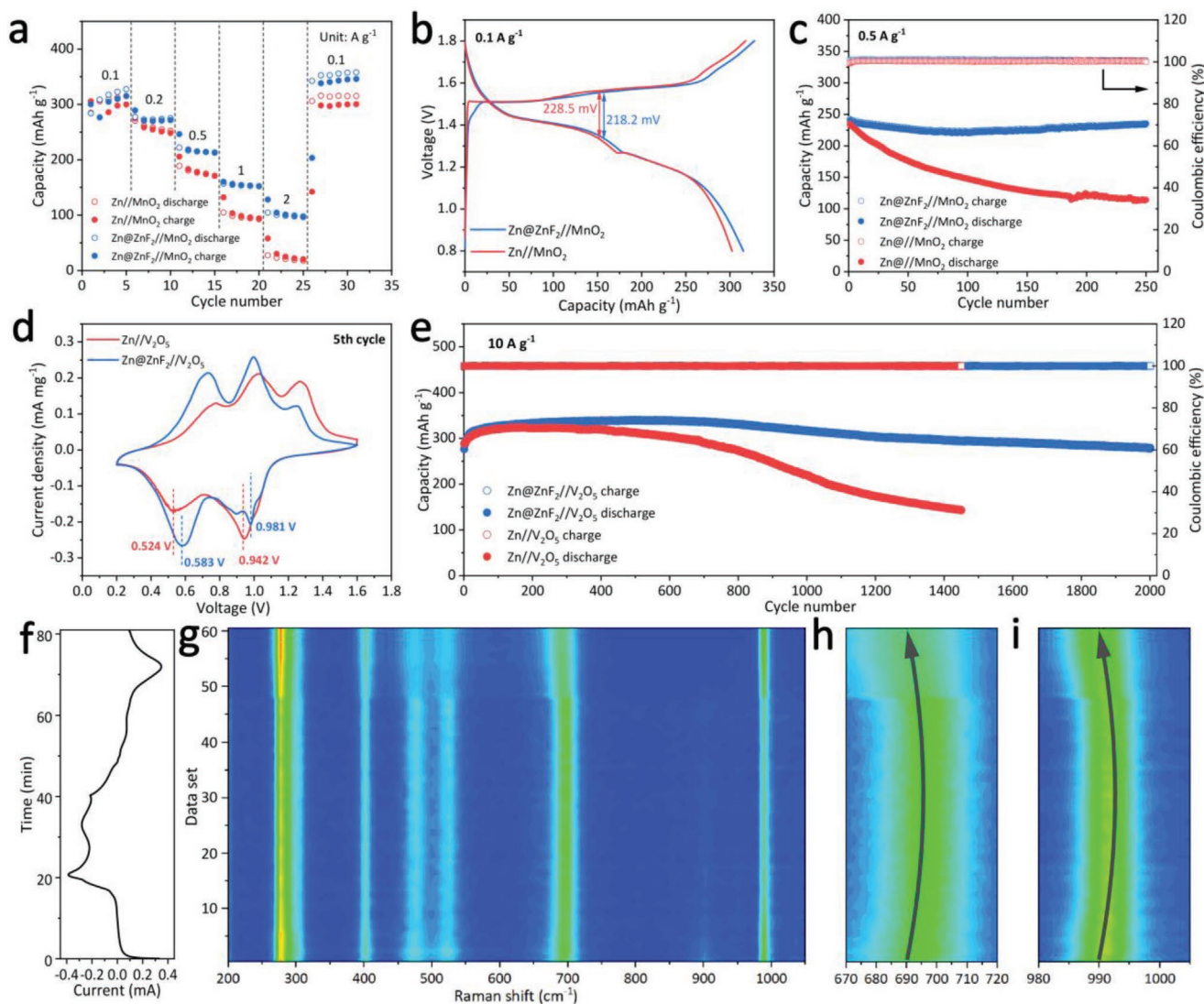


**Figure 5.** a) Rate performance of the Zn//MnO<sub>2</sub> and Zn@ZnF<sub>2</sub>//MnO<sub>2</sub> cells. b) The voltage hysteresis of the Zn//MnO<sub>2</sub> and Zn@ZnF<sub>2</sub>//MnO<sub>2</sub> cells at 0.1 A g<sup>-1</sup>. c) Cycling performance of both cells at 0.5 A g<sup>-1</sup>. d) CV curves of the Zn//V<sub>2</sub>O<sub>5</sub> and Zn@ZnF<sub>2</sub>//V<sub>2</sub>O<sub>5</sub> cells. e) Long-term cycling stability of the Zn//V<sub>2</sub>O<sub>5</sub> and Zn@ZnF<sub>2</sub>//V<sub>2</sub>O<sub>5</sub> cells at 10 A g<sup>-1</sup>. f-i) In situ Raman spectra of the V<sub>2</sub>O<sub>5</sub> cathode cycled with the Zn@ZnF<sub>2</sub> electrode as an anode.

materials to couple with the aforementioned Zn foil and Zn@ZnF<sub>2</sub> anodes to fabricate zinc-ion full batteries (Figure 5). Rate performance of the Zn//MnO<sub>2</sub> and Zn@ZnF<sub>2</sub>//MnO<sub>2</sub> cells are presented in Figure 5a. At the low current density of 0.1 A g<sup>-1</sup>, the Zn//MnO<sub>2</sub> and Zn@ZnF<sub>2</sub>//MnO<sub>2</sub> cells exhibit similar average discharge capacities of 305.4, and 312.0 mAh g<sup>-1</sup>, respectively. As the current density increases stepwise, the Zn@ZnF<sub>2</sub>//MnO<sub>2</sub> cell delivers superior discharge capacities of 274.4, 216.3, 154.1, and 99.6 mAh g<sup>-1</sup> under 0.2, 0.5, 1 and 2 A g<sup>-1</sup>, respectively. As a comparison, the discharge capacity of the Zn//MnO<sub>2</sub> cell quickly decreases to only 21.6 mAh g<sup>-1</sup> at 2 A g<sup>-1</sup>. The voltage hysteresis during cycling (defined as the voltage gap at the half discharge capacity) is a critical indicator to investigate the reversibility of batteries. As shown in Figure 5b, the Zn@ZnF<sub>2</sub>//MnO<sub>2</sub> cell exhibits a lower voltage hysteresis (218.2 mV) than that of the Zn//MnO<sub>2</sub> cell (228.5 mV) at 0.1 A g<sup>-1</sup>. Furthermore, more evident differences in

overpotential for these two cells can be found at the higher current densities (Figure S10, Supporting Information). As shown in Figure 5c, the Zn@ZnF<sub>2</sub>//MnO<sub>2</sub> cell maintains a reversible capacity of 234.8 mAh g<sup>-1</sup> with a CE of 100.4% after 250 cycles at 0.5 A g<sup>-1</sup>, while the Zn//MnO<sub>2</sub> cell exhibits obvious capacity decay (only 100.1 mAh g<sup>-1</sup> is retained after 250 cycles).

Moreover, the cells using commercial V<sub>2</sub>O<sub>5</sub> as the cathode have also been tested. The cyclic voltammetry (CV) curves of the Zn//V<sub>2</sub>O<sub>5</sub> and Zn@ZnF<sub>2</sub>//V<sub>2</sub>O<sub>5</sub> cells at a scan rate of 0.1 mV s<sup>-1</sup> (Figure 5d) imply multistep redox couples of V<sup>4+</sup>/V<sup>3+</sup> and V<sup>5+</sup>/V<sup>4+</sup> induced by ions intercalation/extraction. In the cathodic process, two peaks are present at 0.524 and 0.942 V for the Zn//V<sub>2</sub>O<sub>5</sub> cell, which positively shift to 0.583 and 0.981 V for the Zn@ZnF<sub>2</sub>//V<sub>2</sub>O<sub>5</sub> cell, respectively. The higher reduction potentials imply the smaller polarization for the Zn@ZnF<sub>2</sub>//V<sub>2</sub>O<sub>5</sub> cell. The long-term cycling performance of the Zn//V<sub>2</sub>O<sub>5</sub> and Zn@ZnF<sub>2</sub>//V<sub>2</sub>O<sub>5</sub> cells is presented in



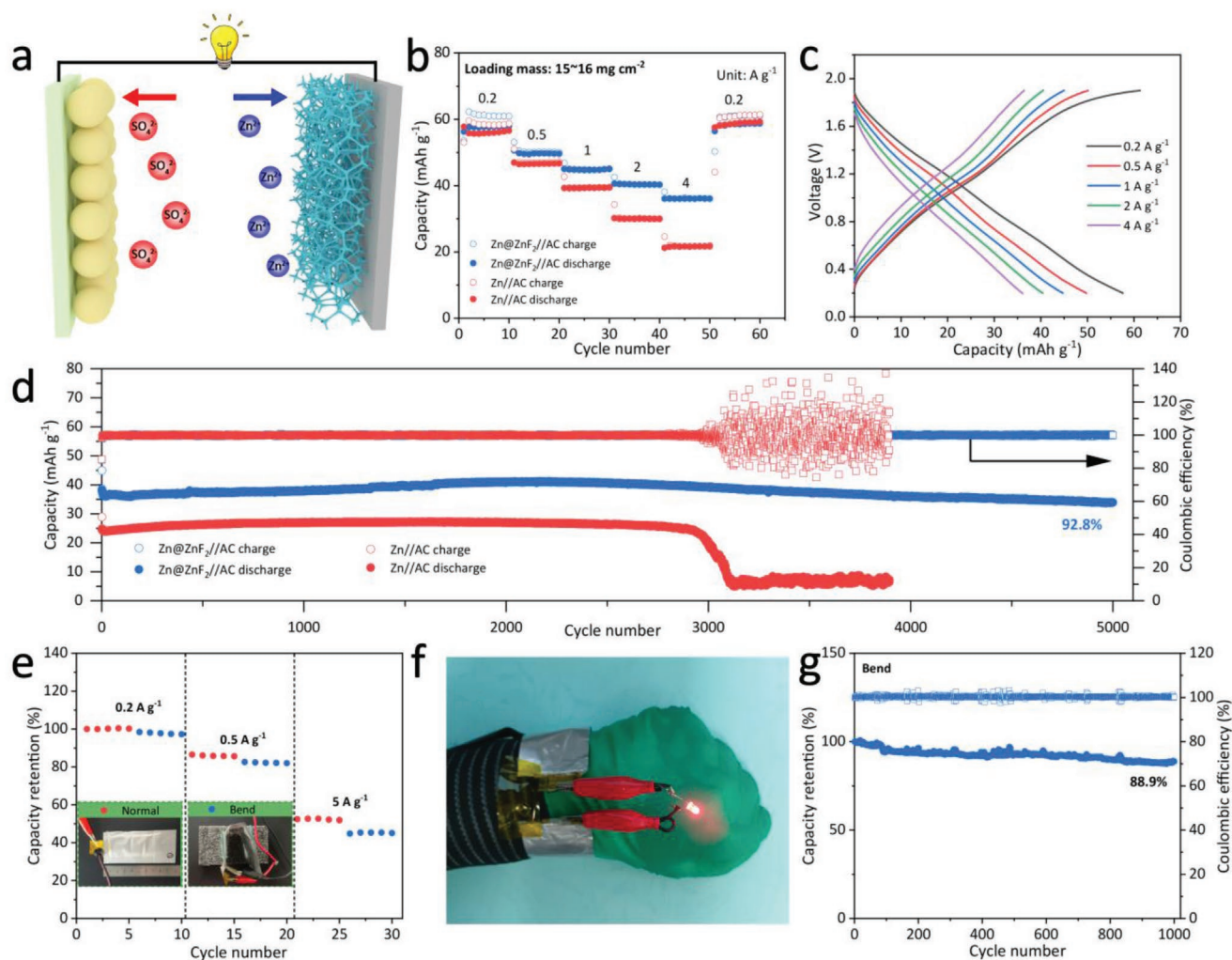


**Figure 6.** Electrochemical performance of the Zn@ZnF<sub>2</sub>//AC hybrid ZICs device. a) Schematic of the Zn@ZnF<sub>2</sub>//AC hybrid ZICs. b) Rate performance of the Zn//AC and Zn@ZnF<sub>2</sub>//AC hybrid ZICs in the voltage range of 0.2–2.0 V. c) Galvanostatic charge/discharge profiles of the Zn@ZnF<sub>2</sub>//AC hybrid ZICs. d) Long-term cycling performance of the Zn//AC and Zn@ZnF<sub>2</sub>//AC hybrid ZICs at the current density of 2 A g<sup>-1</sup>. e) The comparison of capacity retention of the Zn@ZnF<sub>2</sub>//AC hybrid ZICs under flat and bend states cycled at various current densities. f) Optical photograph of a red LED lit by the flexible Zn@ZnF<sub>2</sub>//AC hybrid ZIC on the wrist. g) Cycling stability of the Zn@ZnF<sub>2</sub>//AC hybrid ZICs under bend state at 2 A g<sup>-1</sup>.

Figure 5e. The Zn@ZnF<sub>2</sub>//V<sub>2</sub>O<sub>5</sub> cell achieves an enduring and stable discharge capacity of 279.2 mAh g<sup>-1</sup> with as high as 96.0% capacity retention after 2000 cycles at the high current density of 10 A g<sup>-1</sup>. In comparison, the specific capacity of the Zn//V<sub>2</sub>O<sub>5</sub> cell fades rapidly and the capacity retention is only 49.4% over 1500 cycles. Furthermore, the high loading Zn//V<sub>2</sub>O<sub>5</sub> cell with a limited Zn/V<sub>2</sub>O<sub>5</sub> mass ratio of 1.76 was also investigated, in which Zn foil with 30 μm thickness was used as the starting substrate (Figure S11, Supporting Information). Such a cell can also deliver a considerable reversible capacity of 283.1 mAh g<sup>-1</sup> after 400 cycles at 5 A g<sup>-1</sup>. Additionally, the in situ Raman spectroscopic signal was acquired synchronously with CV operations of the Zn//V<sub>2</sub>O<sub>5</sub> cell at the scan rate of 0.58 mV s<sup>-1</sup> to get deeper insights into its excellent cycling stability (Figure 5f–i). The Raman spectroscopy of pristine V<sub>2</sub>O<sub>5</sub> electrode before cycling shows six obvious peaks at approximately 279, 403, 475, 520, 694 and 991 cm<sup>-1</sup>, which can be attributed to the bending vibration of V2–O bonds, the stretching mode of V3–O, the

double coordinated V2–O stretching mode, and the terminal oxygen (V=O) stretching vibration, respectively.<sup>[32]</sup> The characteristic peaks of V<sub>2</sub>O<sub>5</sub> always remain and no other new peaks are emerged during cycling, indicating that Zn<sup>2+</sup> intercalation/deintercalation in V<sub>2</sub>O<sub>5</sub> does not damage the internal crystal-line structure (Figure 5g). The peaks at 694 cm<sup>-1</sup> (Figure 5h) and 991 cm<sup>-1</sup> (Figure 5i) exhibit a blueshift trend during the discharge process, which may be attributed to the effect of insertion Zn<sup>2+</sup> ions on the vibrational bands. However, all these peaks basically recover to their original positions after cycling, indicating that the structure evolution of the V<sub>2</sub>O<sub>5</sub> cathode occurred during discharge/charge processes is highly reversible and stable in the Zn@ZnF<sub>2</sub>//V<sub>2</sub>O<sub>5</sub> cell, confirming the valid regulation of Zn transport kinetics by introducing the ZnF<sub>2</sub> matrix.

The outstanding high-rate cycling stability of the Zn@ZnF<sub>2</sub>//AC electrode makes it a promising anode candidate for constructing hybrid Zn-ion capacitors (ZICs), in which the Zn@ZnF<sub>2</sub> electrode was used as the battery-type anode

and a home-made active carbon (AC) electrode was used as the capacitor-type cathode (Figure 6a). The ZICs work with  $\text{SO}_4^{2-}$  anions physical absorbing/desorbing onto/from the cathode, and  $\text{Zn}^{2+}$  cations deposition/stripping onto/from the anode simultaneously, which have characteristics of longer cycle life and higher power density than those of conventional ZIBs. Owing to the fast  $\text{Zn}^{2+}$  deposition kinetics, the  $\text{Zn@ZnF}_2/\text{AC}$  hybrid ZIC exhibits a better high rate capability compared with the  $\text{Zn}/\text{AC}$  hybrid ZIC. As shown in Figure 6b, the average reversible capacities of 60.5, 50.5, 45.1, 40.6, and 36.4  $\text{mAh g}^{-1}$  can be retained for the  $\text{Zn@ZnF}_2/\text{AC}$  hybrid ZIC at a current density of 0.2, 0.5, 1, 2, and 4  $\text{A g}^{-1}$ , respectively. It is worth noting that the loading mass of AC in the cathode reaches as high as 15–16  $\text{mg cm}^{-2}$  in this study, the highest gravimetric current density of 4  $\text{A g}^{-1}$  applied at the cathode is translated to an extremely high areal current density of  $\approx 60 \text{ mA cm}^{-2}$ . The voltage profiles at all these current densities are close to the linear shape expected for an ideal supercapacitor (Figure 6c), implying a small polarization in the  $\text{Zn@ZnF}_2/\text{AC}$  hybrid ZIC. Furthermore, the long-term cycling performance of the  $\text{Zn}/\text{AC}$  and  $\text{Zn@ZnF}_2/\text{AC}$  hybrid ZICs is also investigated at a current density of 2  $\text{A g}^{-1}$  (Figure 6d). The  $\text{Zn@ZnF}_2/\text{AC}$  hybrid ZIC shows remarkable capacity retention of  $\approx 92.8\%$  after 5000 cycles with a CE of  $\approx 100\%$ . Nevertheless, the capacity of the  $\text{Zn}/\text{AC}$  hybrid ZIC decays quickly and the CE fluctuates dramatically after 3000 cycles, resulting from the irreversible loss of Zn during repeated cycling.

After coin-cell configuration tests, a flexible aqueous  $\text{Zn@ZnF}_2/\text{AC}$  hybrid ZIC was also fabricated by assembling a  $\text{Zn@ZnF}_2$  electrode, a separator soaked with 2 M  $\text{ZnSO}_4$  aqueous electrolyte, and an AC cathode to form the “sandwich” structure, and then heat-sealing by the aluminum-plastic film. Whether the bending status will affect the electrochemical performance of the flexible  $\text{Zn@ZnF}_2/\text{AC}$  hybrid ZIC was first studied. The flexible  $\text{Zn@ZnF}_2/\text{AC}$  hybrid ZIC was tested for 5 cycles under flat state and for another 5 cycles under bend state by turns (Figure 6e). Experiencing 30 cycles of flat-bent operations, no evident change of the capacity retention collected under normal and bend states can be found at various current densities of 0.2, 0.5, and 5  $\text{A g}^{-1}$ , indicating good mechanical strength and excellent flexibility against repeated bending. Besides, the flexible  $\text{Zn@ZnF}_2/\text{AC}$  hybrid ZIC on the wrist can successfully power up a red LED (Figure 6f), showing its potential application prospect in wearable electronic devices. Moreover, the bend  $\text{Zn@ZnF}_2/\text{AC}$  hybrid ZIC can maintain a high capacity retention of 88.9% after 1000 cycles at 2  $\text{A g}^{-1}$  (Figure 6g), demonstrating its outstanding durability under bend state during prolonged cycling.

In summary, we fabricated a 3D interconnected  $\text{ZnF}_2$  matrix on Zn metal surface through a simple and fast anodic growth strategy. This rational design renders outstanding merits, including improved wettability for aqueous electrolyte, high corrosion resistance, suppressed hydrogen evolution reaction, and improved  $\text{Zn}^{2+}$  desolvation capability. Ex situ SEM, in situ optical microscopy, and COMSOL numerical simulation results reveal that the multifunctional  $\text{ZnF}_2$  matrix can effectively inhibit the formation of Zn dendrites and regulate the Zn deposition kinetics. As a result, the as-fabricated  $\text{Zn@ZnF}_2$  electrode delivers high Coulombic efficiency

( $\approx 99.5\%$ ) and ultralong lifespan (800 h) with a relatively high plating capacity of  $1 \text{ mAh cm}^{-2}$ . Furthermore, the feasibility of the  $\text{Zn@ZnF}_2$  electrode is verified in ZIBs and hybrid ZICs. The  $\text{Zn@ZnF}_2/\text{V}_2\text{O}_5$  ZIB can maintain a stable capacity of  $279.2 \text{ mAh g}^{-1}$  with as high as 96.0% capacity retention after 2000 cycles at  $10 \text{ A g}^{-1}$ , and the  $\text{Zn@ZnF}_2/\text{AC}$  hybrid ZIC shows a long cycle life of 5000 cycles. The work is expected to open new avenues in the development of high-performance Zn metal anodes, and provides great opportunities for realizing the practical applications of aqueous zinc-ion batteries and capacitors.

## Supporting Information

Supporting Information is available from the Wiley Online Library or from the author.

## Acknowledgements

This work was supported by Guangdong Province Basic and Applied Basic Research Fund (No. 2019A1515111069) and National Natural Science Foundation of China (No. 51771058).

## Conflict of Interest

The authors declare no conflict of interest.

## Data Availability Statement

Research data are not shared.

## Keywords

aqueous zinc-ion batteries, desolvation effect, Zn metal anodes,  $\text{Zn}^{2+}$  ion flux,  $\text{ZnF}_2$  matrix

Received: October 28, 2020  
Revised: December 28, 2020  
Published online: February 8, 2021

- [1] J. M. Tarascon, M. Armand, *Nature* **2001**, 414, 359.
- [2] C. Yang, J. Chen, T. Qing, X. Fan, W. Sun, A. von Cresce, M. S. Ding, O. Borodin, J. Vatamanu, M. A. Schroeder, N. Eidson, C. Wang, K. Xu, *Joule* **2017**, 1, 122.
- [3] a) C. Yang, J. Chen, X. Ji, T. P. Pollard, X. Lü, C.-J. Sun, S. Hou, Q. Liu, C. Liu, T. Qing, Y. Wang, O. Borodin, Y. Ren, K. Xu, C. Wang, *Nature* **2019**, 569, 245; b) R. Demir-Cakan, M. R. Palacin, L. Croguennec, *J. Mater. Chem. A* **2019**, 7, 20519; c) G. Fang, J. Zhou, A. Pan, S. Liang, *ACS Energy Lett.* **2018**, 3, 2480.
- [4] C. Xia, J. Guo, Y. Lei, H. Liang, C. Zhao, H. N. Alshareef, *Adv. Mater.* **2018**, 30, 1705580.
- [5] a) L. E. Blanc, D. Kundu, L. F. Nazar, *Joule* **2020**, 4, 771; b) X. Zeng, J. Hao, Z. Wang, J. Mao, Z. Guo, *Energy Storage Mater.* **2019**, 20, 410.



- [6] Q. Zhang, J. Luan, L. Fu, S. Wu, Y. Tang, X. Ji, H. Wang, *Angew. Chem., Int. Ed.* **2019**, 58, 15841.
- [7] Z. Liu, T. Cui, G. Pulletikurthi, A. Lahiri, T. Carstens, M. Olschewski, F. Endres, *Angew. Chem., Int. Ed.* **2016**, 55, 2889.
- [8] N. Wang, Y. Yang, X. Qiu, X. L. Dong, Y. G. Wang, Y. Y. Xia, *ChemSusChem* **2020**, 13, 5556.
- [9] X. Liu, O. Bolton, R. Akolkar, *J. Electrochem. Soc.* **2019**, 166, D583.
- [10] K. L. Liu, P. He, H. M. Bai, J. C. Chen, F. Q. Dong, S. B. Wang, M. Q. He, S. P. Yuan, *Mater. Chem. Phys.* **2017**, 199, 73.
- [11] J. Q. Huang, X. W. Chi, Q. Han, Y. Z. Liu, Y. X. Du, J. H. Yang, Y. Liu, *J. Electrochem. Soc.* **2019**, 166, A1211.
- [12] W. Xu, K. Zhao, W. Huo, Y. Wang, G. Yao, X. Gu, H. Cheng, L. Mai, C. Hu, X. Wang, *Nano Energy* **2019**, 62, 275.
- [13] F. Wang, O. Borodin, T. Gao, X. Fan, W. Sun, F. Han, A. Faraone, J. A. Dura, K. Xu, C. Wang, *Nat. Mater.* **2018**, 17, 543.
- [14] a) X. Wu, Y. Xu, C. Zhang, D. P. Leonard, A. Markir, J. Lu, X. Ji, *J. Am. Chem. Soc.* **2019**, 141, 6338; b) C. Zhang, J. Holoubek, X. Wu, A. Daniyar, L. Zhu, C. Chen, D. P. Leonard, I. A. Rodriguez-Perez, J.-X. Jiang, C. Fang, X. Ji, *Chem. Commun.* **2018**, 54, 14097.
- [15] J. Zhao, J. Zhang, W. Yang, B. Chen, Z. Zhao, H. Qiu, S. Dong, X. Zhou, G. Cui, L. Chen, *Nano Energy* **2019**, 57, 625.
- [16] Z. M. Zhao, J. W. Zhao, Z. L. Hu, J. D. Li, J. J. Li, Y. J. Zhang, C. Wang, G. L. Cui, *Energy Environ. Sci.* **2019**, 12, 1938.
- [17] a) H. Yang, Y. Qiao, Z. Chang, H. Deng, P. He, H. Zhou, *Adv. Mater.* **2020**, 32, 2004240; b) Z. Q. Wang, J. T. Hu, L. Han, Z. J. Wang, H. B. Wang, Q. H. Zhao, J. J. Liu, F. Pan, *Nano Energy* **2019**, 56, 92; c) H. Yang, Z. Chang, Y. Qiao, H. Deng, X. Mu, P. He, H. Zhou, *Angew. Chem., Int. Ed.* **2020**, 59, 9377.
- [18] L. T. Kang, M. W. Cui, F. Y. Jiang, Y. F. Gao, H. J. Luo, J. J. Liu, W. Liang, C. Y. Zhi, *Adv. Energy Mater.* **2018**, 8, 1801090.
- [19] J. Hao, X. Li, S. Zhang, F. Yang, X. Zeng, S. Zhang, G. Bo, C. Wang, Z. Guo, *Adv. Funct. Mater.* **2020**, 30, 2001263.
- [20] a) J. Y. Kim, G. Liu, G. Y. Shim, H. Kim, J. K. Lee, *Adv. Funct. Mater.* **2020**, 30, 2004210; b) X. Xie, S. Liang, J. Gao, S. Guo, J. Guo, C. Wang, G. Xu, X. Wu, G. Chen, J. Zhou, *Energy Environ. Sci.* **2020**, 13, 503.
- [21] J. Hao, B. Li, X. Li, X. Zeng, S. Zhang, F. Yang, S. Liu, D. Li, C. Wu, Z. Guo, *Adv. Mater.* **2020**, 32, 2003021.
- [22] A. Wang, W. Zhou, A. Huang, M. Chen, J. Chen, Q. Tian, J. Xu, *J. Colloid Interface Sci.* **2020**, 577, 256.
- [23] K. Hu, X. Guan, R. Lv, G. Li, Z. Hu, L. Ren, A. Wang, X. Liu, J. Luo, *Chem. Eng. J.* **2020**, 396, 125363.
- [24] R. Zhao, Y. Yang, G. Liu, R. Zhu, J. Huang, Z. Chen, Z. Gao, X. Chen, L. Qie, *Adv. Funct. Mater.* **2021**, 31, 2001867.
- [25] Z. Hong, Z. Ahmad, V. Viswanathan, *ACS Energy Lett.* **2020**, 5, 2466.
- [26] W. Yang, X. Du, J. Zhao, Z. Chen, J. Li, J. Xie, Y. Zhang, Z. Cui, Q. Kong, Z. Zhao, C. Wang, Q. Zhang, G. Cui, *Joule* **2020**, 4, 1557.
- [27] a) N. K. Shrestha, R. Hahn, K. Lee, A. Tighineanu, P. Schmuki, *ECS Electrochem. Lett.* **2013**, 3, E1; b) H. Y. Xu, Y. C. Liu, R. Mu, C. L. Shao, Y. M. Lu, D. Z. Shen, X. W. Fan, *Appl. Phys. Lett.* **2005**, 86, 123107.
- [28] J. Wang, Z. Cai, R. Xiao, Y. Ou, R. Zhan, Z. Yuan, Y. Sun, *ACS Appl. Mater. Interfaces* **2020**, 12, 23028.
- [29] J. Shin, J. Lee, Y. Park, J. W. Choi, *Chem. Sci.* **2020**, 11, 2028.
- [30] Y. Zhang, Z. Chen, H. Qiu, W. Yang, Z. Zhao, J. Zhao, G. Cui, *NPG Asia Mater.* **2020**, 12, 4.
- [31] H. Qiu, X. Du, J. Zhao, Y. Wang, J. Ju, Z. Chen, Z. Hu, D. Yan, X. Zhou, G. Cui, *Nat. Commun.* **2019**, 10, 5374.
- [32] a) T. Wei, Q. Li, G. Yang, C. Wang, *J. Mater. Chem. A* **2018**, 6, 8006; b) P. He, Y. Quan, X. Xu, M. Yan, W. Yang, Q. An, L. He, L. Mai, *Small* **2017**, 13, 1702551; c) J. Lee, S. Badie, P. Srimuk, A. Ridder, H. Shim, S. Choudhury, Y. C. Nah, V. Presser, *Sustainable Energy Fuels* **2018**, 2, 577.